

SonarSplat: Novel View Synthesis of Imaging Sonar via Gaussian Splatting

Advait V. Sethuraman¹
Pou-Chun Kung¹

Max Rucker¹
Nibarkavi N.B. Amutha¹

Onur Bagoren¹
Katherine A. Skinner¹

¹Department of Robotics, University of Michigan, Ann Arbor

Abstract

In this paper, we present *SonarSplat*, a novel Gaussian splatting framework for imaging sonar that demonstrates realistic novel view synthesis and models acoustic streaking phenomena. Our method represents the scene as a set of 3D Gaussians with acoustic reflectance and saturation properties. We develop a novel method to efficiently rasterize learned Gaussians to produce a range/azimuth image that is faithful to the acoustic image formation model of imaging sonar. In particular, we develop a novel approach to model azimuth streaking in a Gaussian splatting framework. We evaluate *SonarSplat* using real-world datasets of sonar images collected from an underwater robotic platform in a controlled test tank and in a real-world river environment. Compared to the state-of-the-art, *SonarSplat* offers improved image synthesis capabilities (+2.5 dB PSNR). We also demonstrate that *SonarSplat* can be leveraged for azimuth streak removal and 3D scene reconstruction.

1. Introduction

Acoustic sensors, such as imaging sonar, are commonly used for infrastructure inspection, large-area mapping, and target detection in underwater environments [12, 20, 34]. Unlike optical sensors, which are severely range-limited due to water column effects on light propagation, acoustic sensors can capture data at long ranges to provide critical information about subsea environments. Although sonar exhibits many desirable qualities such as longer range, invariance to lighting conditions, and the ability to discern material properties, there exist acoustic phenomena, including elevation ambiguity, azimuth streaking, and multi-path reflections, which make sonar interpretation difficult for operators and computer vision algorithms alike. Furthermore, the severe lack of large, public datasets for sonar slows progress in traditional computer vision tasks like object detection, segmentation, and reconstruction.

Recently, neural radiance fields (NeRFs) [22] have

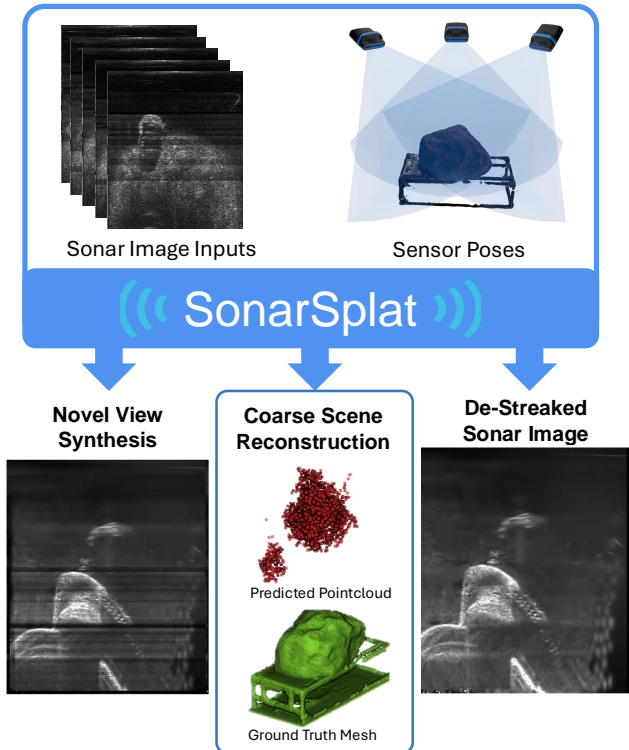


Figure 1. We present *SonarSplat*, a method that uses posed sonar images to produce a novel 3D Gaussian Splat representation that enables novel view synthesis of realistic sonar images and coarse 3D reconstruction. With *SonarSplat*, the scene is represented with a set of 3D Gaussians that model the reflectivity and azimuth streaking probabilities of objects in the rendering process. This novel formulation enables additional features of *SonarSplat*, such as azimuth streak removal, enabling the recovery of clean sonar images from saturated ones.

demonstrated the potential for high-fidelity data synthesis and denoising of optical imagery [6, 27]. The benefits of neural rendering have been recognized by the underwater perception community, with prior work exploring neural rendering for 3D object reconstruction using underwater

cameras [15, 35] and sonar data [7, 30, 31, 43, 44]. While these innovations are promising, training and processing NeRFs is extremely costly and time-consuming, making deploying them in real-time or on resource-constrained devices difficult. More recently, 3D Gaussian splatting (3DGS) [13] was developed as a faster alternative to NeRF. 3DGS utilizes sparse points in the form of 3D Gaussians to represent the scene. This allows 3DGS to preserve properties of continuous volumetric radiance fields while lowering computational costs. Gaussian splatting has been leveraged for underwater imagery [16, 23, 45]. Most relevant to our proposed work, ZSplat proposes a Gaussian splatting framework for RGB-sonar fusion [32]. However, ZSplat leverages the fusion of sonar data to improve the rendering of RGB images and does not focus on enabling high-fidelity data synthesis for sonar imagery or provide evaluation for the quality of rendered sonar images. Thus, there is a clear gap in the literature for a framework capable of efficient and effective sonar image synthesis.

In this paper, we propose SonarSplat (Fig. 1), a novel Gaussian splatting framework for imaging sonar that enables efficient and high quality novel view synthesis for imaging sonar data. We focus on modeling characteristic acoustic noise properties, specifically, azimuth streaking, or receiver saturation, which can make image interpretation and 3D reconstruction difficult. By modeling realistic noise effects, we demonstrate that we can leverage SonarSplat to perform efficient, high quality sonar image synthesis and noise removal. Lastly, we also demonstrate SonarSplat’s ability to learn geometry of the scene, overcoming the elevation ambiguity inherent in imaging sonar image formation. Our main contributions are summarized as follows:

- We develop a novel 3D Gaussian splatting framework for rasterization of range/azimuth sonar images from known and novel viewpoints.
- We develop a novel method for learning the probability of azimuth streaking in a differentiable manner, which allows for removal of unwanted azimuth streaking artifacts from rendered images.
- We perform quantitative and qualitative evaluation of our method on real imaging sonar data collected from a robotic platform with a variety of sonar ranges and environments.

Code and data will be made publicly available on a project website after a double-blind review.

2. Related Work

2.1. Radiance Field Methods

NeRFs represent scenes implicitly using neural networks and have been explored for a variety of applications, including novel view synthesis, inverse rendering, data generation, and image denoising [6, 8, 21, 27]. Later works improved

NeRFs through improved sampling of the volumetric representation and improvements in rendering speed with alternative encoding methods [2, 24]. Despite their vast success as a learned scene representation, a key struggle for the practical application of NeRFs is the long training time and the slow rendering speeds, primarily due to the computationally expensive volumetric rendering process [21]. A recent development in radiance field methods is Gaussian splatting, which uses *rasterization* instead of volumetric rendering to optimize and produce a scene representation [13]. The resulting renders from 3DGS are both high in quality and reach unprecedented rendering speeds, enabling fast rendering for various real-time applications [18, 19].

Despite their impressive performance and rapid adoption, radiance field methods were developed with optical sensors in mind, limiting their direct application to non-visual sensors. Recent developments have integrated the physics-based image formation models of various non-visual sensors, including radar, LIDAR, sonar, thermal cameras, and event cameras into NeRF and Gaussian splatting frameworks for various vision tasks [3, 4, 10, 17, 30]. In this work, we propose a novel Gaussian splatting framework for imaging sonar for underwater applications.

2.2. Perception Challenges for Imaging Sonar

Imaging sonar is a popular underwater sensor for perception tasks like object detection, segmentation, reconstruction, and inspection [9, 12, 25, 30, 38]. The key challenges with working with imaging sonars for these tasks are properties inherent with the acoustic image formation model [29]. The sensor is susceptible to multi-path effects, highly nonlinear noise patterns, and phenomena like azimuth streaking [28]. Azimuth streaking, in particular, can make sonar image understanding difficult by suppressing returns from certain azimuth angles, causing black bars in the sonar image [28]. In addition, the sensor inherently loses information from 3D into 2D when capturing the acoustic returns, causing an effect known as elevation ambiguity [40]. This ambiguity has made the successful application of imaging sonar to 3D vision tasks difficult [11, 25, 42]. Yet, imaging sonars still remain an extremely valuable sensor for underwater imaging, especially in long range imaging and deep water applications where optical sensors may fail [39].

Given its importance to underwater perception, prior work has proposed sonar simulators to validate perception algorithms without the cost, time commitment, and difficulty of real-world data collection [5, 29]. Although these works model complex interactions with the environment, such as multi-path reflections and azimuth streaking, there still exists a *sim-to-real gap* inherent with simulators. Furthermore, simulators also require the manual tuning of acoustic and scene parameters to match the distribution of data desired by the end-user. Rather, our pro-

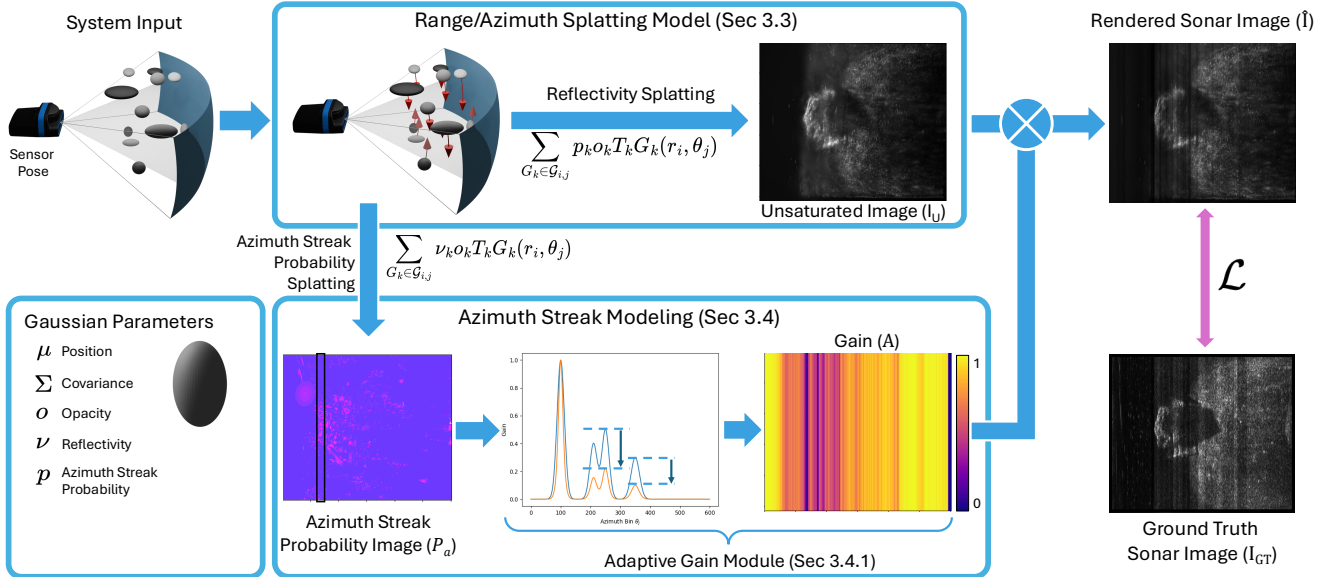


Figure 2. Overview of SonarSplat. Our method takes as input a sensor pose and an initial set of 3D Gaussians representing the scene. Then, we transform the 3D Gaussians into the sensor’s image space. We splat the reflectivity parameter ν_k to get the unsaturated image I_u . Additionally, we optimize and splat per-Gaussian azimuth streaking probabilities p_k . All the probabilities in range interval r_i are considered in our novel Adaptive Gain Module, which adjusts the receiver gain applied to I_u . Finally, we produce \hat{I} by multiplying the gain A by I_u . All parameters are optimized using gradient descent by taking losses with respect to the sonar image pixel values. All sonar images shown are polar (range-azimuth) coordinates.

posed work proposes a Gaussian splatting framework that can learn from real data to produce realistic sonar data from novel poses, which may be useful for augmenting datasets and addressing the data scarcity problem.

2.3. Novel View Synthesis for Imaging Sonar

Prior work has incorporated the sonar image formation model into signed distance field (SDF) and NeRF formulations [7, 30]. Neusis [30] presents a NeRF framework for dense 3D reconstruction of objects using an imaging sonar, specifically, a forward-looking sonar (FLS). Neusis proposes a differentiable volumetric renderer to model the propagation of acoustic waves to synthesize imaging sonar measurements. By using this implicit representation and multiple sensor measurements, Neusis attempts to resolve the elevation ambiguity present in the image data to construct a 3D mesh of the environment. Neusis-NGP [44] is an extension of Neusis that leverages multi-resolution hash encodings to produce a bathymetric heightmap of the environment. To perform novel view synthesis with Neusis and Neusis-NGP, every 2D pixel that makes up a sonar image is sampled along its elevation ambiguity and then evaluated by the rendering networks to determine the intensity of each point. These points are then summed to extract the return at the specific pixel coordinate. We show that this process is time-consuming and does not produce photorealistic sonar imagery. Differentiable Space Carving (DSC) [7] proposes

a faster method that models echo probabilities to carve out a mesh of the scene. This method is similar to Neusis, but avoids having to implicitly represent the scene as intensities. While this method is faster, it still requires sampling points at every pixel and then evaluating the occupancy to perform sonar novel view synthesis. Through our experiments, we show that DSC is also unable to produce high-quality novel view synthesis of imaging sonar.

Following recent developments in 3DGS, Z-Splat [32] introduces a novel method for fusing camera and sonar data, enhancing RGB image rendering by incorporating depth supervision from sonar returns. To the best of our knowledge, Z-Splat [32] is the only Gaussian splatting paper that incorporates acoustic sensor data, with demonstrations on underwater data. This is done by splatting Gaussians onto the X/Z plane and calculating a depth loss between the sonar returns and the splatted Gaussians. While this process improves the placement of Gaussians for better camera renderings, Z-Splat oversimplifies the splatting process by not accounting for any sonar-specific phenomena. More importantly, Z-Splat only splats the *opacities* of Gaussians, and does not consider material properties like acoustic reflectance. This leads to poor sonar renderings, which limit its application to sonar novel view synthesis. We demonstrate that SonarSplat, using *range-azimuth* splatting, produces more accurate novel view synthesis and can also restore sonar images to remove azimuth streaking artifacts.

3. Technical Approach

Fig. 2 shows an overview of SonarSplat, which uses sonar images and their corresponding sensor poses to optimize a scene representation. The scene is represented as a set of 3D Gaussian primitives, each parametrized with a mean, covariance, opacity, acoustic reflectivity and azimuth streaking probability. First, the Gaussians that fall within the view frustum of the sonar are rasterized into a range-azimuth image. Concurrently, we render an azimuth streak probability image using the per-Gaussian azimuth streak probabilities. Based on the relative probabilities in each range bin, we use a novel adaptive gain module to adjust the acoustic returns and capture azimuth streaking effects. Finally, we produce a sonar image with azimuth streaks that can be optimized by taking a loss with respect to the ground truth sonar image. We provide further detail of each of these components in the remainder of this section.

3.1. Gaussian Splatting Primer

This section provides background information about traditional Gaussian splatting for optical images. The standard 3D Gaussian splatting framework models the scene using a set of N 3D Gaussian basis functions, $\mathcal{G} = \{G_i\}_{i=1}^N$, each parametrized with a mean $\mu_i \in \mathbb{R}^3$, scaling $s_i \in \mathbb{R}^3$, quaternion $q_i \in \mathbb{R}^4$, opacity $o_i \in \mathbb{R}$, color $c_i \in \mathbb{R}^3$, encoded as spherical harmonics [13]. In this work, we augment this parametrization with acoustic-specific variables: acoustic reflectivity ν_i and azimuth streak probability p_i . The covariance matrix is constructed from the rotation, q_i , and scaling, s_i , of each Gaussian, each of which is converted to a rotation matrix, $R_i \in \mathbb{R}^{3 \times 3}$, and scaling matrix, $S_i \in \mathbb{R}^{3 \times 3}$ [13]:

$$\Sigma_i = R_i S_i S_i^T R_i^T \quad (1)$$

At a given camera pose $W \in SE(3)$, an image I_G can be rendered in a differentiable manner using a point-based rasterizer. The color, C , at a pixel, p , is computed by blending \hat{N} sorted Gaussians that overlap that pixel:

$$C(p) = \sum_{i=1}^{\hat{N}} c_i o_i T_i G_i \quad (2)$$

where $T_i = \prod_{j=1}^{i-1} (1 - o_j G_j)$ is the transmittance of the Gaussian G_i . The scene is optimized by computing the loss, \mathcal{L}_{GS} , between the rendered image I_G with the ground truth image I_{GT} , through summing L_1 loss and SSIM loss, \mathcal{L}_{SSIM} , as follows:

$$\mathcal{L}_{GS} = \|I_G(W) - I_{GT}(W)\|_1 + \mathcal{L}_{SSIM}(I_G(W), I_{GT}(W)) \quad (3)$$

3.2. Imaging Sonar Image Formation Model

To adapt the optical Gaussian splatting framework to accommodate imaging sonar, we must incorporate the acoustic image formation model. Imaging sonars emit acoustic energy from a transmitter then listen for returns on the receiver. Imaging sonar is a time-of-flight sensor that can provide the echo intensities at a given range and azimuth bin. Importantly, imaging sonar is not able to distinguish the elevation angle of a return, leading to an elevation angle ambiguity. This ambiguity makes direct use of imaging sonar difficult for 3D reconstruction and triangulation tasks [11, 41].

A sonar image is defined as $I \in \mathbb{R}^{N_r \times N_a}$ where N_r denotes the number of range bins, and N_a denotes the number of azimuth bins. In spherical coordinates, the sonar has a vertical field of view (ϕ_{min}, ϕ_{max}) , a horizontal field of view $(\theta_{min}, \theta_{max})$, and a maximum range, R_{max} . Finally, taking $\frac{R_{max}}{N_r}$ gives us the range resolution, ϵ_r , and taking $\frac{\theta_{max} - \theta_{min}}{N_a}$ gives us the azimuthal resolution, ϵ_a .

We leverage the sonar rendering equation introduced in [30], which calculates the intensity of return at bin (r_i, θ_j) in the sonar image I by:

$$I(r_i, \theta_j) = \int_{\phi_{min}}^{\phi_{max}} \int_{\theta_j - \epsilon_a}^{\theta_j + \epsilon_a} \int_{r_i - \epsilon_r}^{r_i + \epsilon_r} \frac{E_e}{r} T(r, \theta, \phi) \sigma(r, \theta, \phi) dr d\theta d\phi \quad (4)$$

where E_e is the intensity of emitted sound, r is the range of the point, $T(r, \theta, \phi)$ is the transmittance term, and $\sigma(r, \theta, \phi)$ is the density of the point. Note that this transmittance term is equivalent to the term used in volumetric rendering such that T serves as the probability that a ray travels to point (r, θ, ϕ) without hitting another particle.

3.3. Range/Azimuth Splatting Model

To evaluate this integral, prior methods use sampling and quadrature [7, 30, 31]. However, motivated by the increased efficiency of splatting techniques, we explore a point-based approach adapted to the sonar image formation model. To this end, we represent the scene with a set of 3D Gaussian primitives $\mathcal{G} = \{G_i\}_{i=1}^N$. Each of these Gaussians are parametrized with a mean $\mu_i \in \mathbb{R}^3$, scale $s_i \in \mathbb{R}^3$, orientation $q_i \in \mathbb{R}^4$, opacity $o_i \in \mathbb{R}$, acoustic reflectivity $\nu_i \in \mathbb{R}$, and azimuth streak probability $p_i \in \mathbb{R}$:

$$G_i = \{\mu_i, s_i, q_i, o_i, \nu_i, p_i\} \quad (5)$$

where the covariance is computed as shown in Eq. (1).

To render sonar images, we first transform the means and covariances of the Gaussians into spherical coordinates. For a given 3D Gaussian in the sensor local frame in Cartesian coordinates, $G_k = \{\mu_k = \langle x_k, y_k, z_k \rangle, \Sigma_k\}$, the transformation to spherical coordinates is as follows [14]:

$$\mu_s = \begin{bmatrix} r_k \\ \theta_k \\ \phi_k \end{bmatrix} = \begin{bmatrix} \|\mu_k\| \\ \arctan(y_k, x_k) \\ \arctan(z_k, \sqrt{x_k^2 + y_k^2}) \end{bmatrix} \quad (6)$$

The covariance Σ_k is transformed by using a first-order linearization of the coordinate transformation, which the Jacobian describes:

$$J_s = \begin{bmatrix} \frac{x_k}{\|\mu_k\|} & \frac{y_k}{\|\mu_k\|} & \frac{z_k}{\|\mu_k\|} \\ \frac{-y}{x^2+y^2} & \frac{x}{x^2+y^2} & 0 \\ \frac{-x_k \cdot z_k}{\|\mu_k\|^2 \sqrt{x^2+y^2}} & \frac{-y_k \cdot z_k}{\|\mu_k\|^2 \sqrt{x^2+y^2}} & \frac{\sqrt{x^2+y^2}}{\|\mu_k\|^2} \end{bmatrix} \quad (7)$$

and the covariance matrix becomes

$$\Sigma_s = J_s \Sigma_k J_s^T \quad (8)$$

To convert the spherical coordinate mean and covariance into range/azimuth image space, we first specify the intrinsic matrix K of the sonar,

$$K = \begin{bmatrix} \frac{1}{\epsilon_r} & 0 & 0 \\ 0 & \frac{1}{\epsilon_a} & \frac{N_a}{2} \\ 0 & 0 & 1 \end{bmatrix} \quad (9)$$

and then we perform the transformation

$$\mu' = K \mu_s, \quad \Sigma' = J_K W \Sigma_s W J_K^T \quad (10)$$

where J_K is the Jacobian of K , and W is the sensor's view matrix, similar to the camera splatting formulation [13].

To find the intensity of acoustic returns at a given range-azimuth bin (r_i, θ_j) , we consider $\mathcal{G}_{i,j} \subset \mathcal{G}$, the set of Gaussians transformed to range-azimuth image space that overlap with the range-azimuth bin (r_i, θ_j) . The rasterization equation to obtain the sonar image for SonarSplat is similar to that of [13], with a few key differences. SonarSplat's rasterization equation is given by:

$$I_U(r_i, \theta_j) = \sum_{G_k \in \mathcal{G}_{i,j}} \nu_k o_k T_k G_k(r_i, \theta_j) \quad (11)$$

where we introduce $\nu_k \in [0, 1]$ as the acoustic reflectance of the Gaussian and T_k as the transmittance from the sensor origin to the Gaussian along the range. The subscript indicates that I_U is the *unsaturated* image, meaning that it does not account for the azimuth streaking that causes saturation across the image. We observe that the acoustic reflectance of a set of points depends on material properties and viewing angle, so ν_k uses spherical harmonics to encode view-dependent effects.

3.4. Modeling Azimuth Streaking

Azimuth streaking, as shown in Fig. 3, is a phenomena that is frequently observed in sonar images. It is a form of saturation that occurs when the sonar receiver receives strong returns from incident angles close to parallel at a specific range bin r_i [29]. The azimuth streaking model found in [29] proposes to modify all the returns in a range interval if

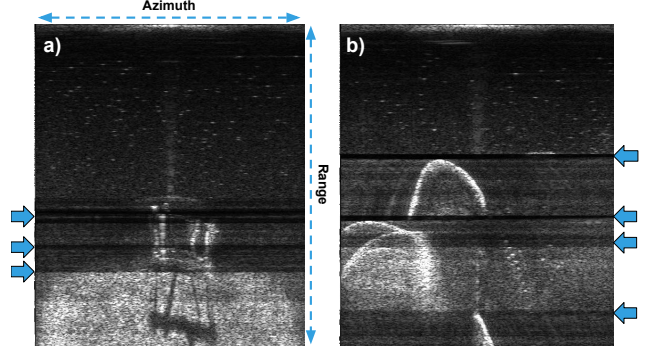


Figure 3. Azimuth streaking is characterized by black streaks (referred to by blue arrows) spanning the azimuth axis of a sonar image. (a) Sonar image of a metal frame structure that experiences azimuth streaking. (b) Sonar image of a concrete piling that has multiple azimuth streaks. Image brightness was enhanced for illustrative purposes. Images are polar (range/azimuth).

a certain percentage of returns exceeds a given threshold ζ . The image with added azimuth streaks is given by:

$$\hat{I}(r_i, \cdot) = 1 - (1 - I(r_i, \cdot))^2 \quad (12)$$

where $\hat{I}(r_i, \cdot)$ is the streaked image, and $I(r_i, \cdot)$ is the vector of intensities at range interval r_i .

In our model, we assign each Gaussian a probability that it will cause an azimuth streak. During the splatting process, we accumulate this probability as a function of the Gaussian's opacity, mean, and covariance. The benefit of defining this probability per-Gaussian is that it can be optimized to produce azimuth streaks that are multi-view consistent.

Let $p_k \in [0, 1]$ be the probability that Gaussian k will contribute to an azimuth streaking phenomena. We can then splat these per-Gaussian probabilities into a range-azimuth bin to obtain an azimuth streak probability image P_a :

$$P_a(r_i, \theta_j) = \sum_{G_k \in \mathcal{G}_{i,j}} p_k o_k T_k G_k(r_i, \theta_j) \quad (13)$$

$$M_a(r_i) = \sum_{\theta=0}^{N_a} P_a(r_i, \theta) \quad (14)$$

where $M_a(r_i)$ represents the probability of an azimuth streak occurring at range interval r_i . The azimuth streak probabilities across the range bins are then used to compute the final image using an adaptive gain mechanism.

3.4.1. Adaptive Gain Module

We introduce a novel adaptive gain term, A , to transform the azimuth streak probability image into receiver gains. We begin designing this gain term with a few observations. First, when no Gaussian in a range bin r_i has a high probability of azimuth streaking, the gain should be unity. Sec-

only, suppose a single Gaussian G_k exhibits a high probability of azimuth streaking across the range bin r_i . In that case, we wish to adaptively *suppress* the other Gaussians in r_i and assign a high gain to G_k . Finally, if multiple Gaussians in r_i have high probabilities of contributing to an azimuth streak, higher gain should be assigned to those Gaussians. To address these observations, the adaptive gain term is applied to each range-azimuth bin (r_i, θ_j) :

$$A(r_i, \theta_j) = P_a(r_i, \theta_j) M_a(r_i) \frac{e^{\gamma P_a(r_i, \theta_j)} + 1}{e^\gamma + 1} + (1 - M_a(r_i)) \quad (15)$$

where γ is a scaling factor that dictates the steepness of the adaptive gain. This behavior aligns with the insight presented in [29]: if a certain percentage of returns exceeds a threshold, an operation is applied to all the values in a range interval. However, our proposed model differs because we do not restrict the gain to a fixed function (quadratic) but rather offer a family of curves for our splatting model to explore during optimization. Further discussion on the adaptive gain term can be found in the supplementary material.

The final image with the azimuth streaks is then computed by applying the gain $A(r_i, \theta_j)$ to its corresponding bin on $I_U(r_i, \theta_j)$:

$$\hat{I}(r_i, \theta_j) = A(r_i, \theta_j) \cdot I_U(r_i, \theta_j) \quad (16)$$

resulting in the final rendered sonar image $\hat{I}(r_i, \theta_j)$.

3.5. Model Optimization

We optimize for desired parameters using SGD and by taking losses (\mathcal{L}_{l1} , \mathcal{L}_{ssim}) between \hat{I} and the ground truth image I_{GT} [13]. To properly optimize for the azimuth streaking probabilities p_k of each Gaussian, we first identify where azimuth streaks occur by calculating the average intensity of the range interval r_i . Then, for the first N_s iterations, we train only on pixels in range bins that exceed a certain average intensity threshold τ . Importantly, p_k is not optimized during this interval. Then, after N_s iterations, we train only on pixels less than τ . We do not optimize μ_k , Σ_k , o_k , or r_k during this interval. This way, we allow the Gaussians to initialize and fit the images before isolating and optimizing the azimuth streaking parameters.

We also encourage each Gaussian to have either high or low opacity via an opacity loss \mathcal{L}_o . This prevents a set of medium-opacity Gaussians from producing the same pixel intensity. Rather, the model is encouraged to use the reflectance parameter r_k to represent low-intensity returns. We use the negative log-likelihood of two Laplacian distributions as in [15].

$$\mathcal{L}_o(x) = |x| |1 - x| \quad (17)$$

The final loss becomes:

$$\mathcal{L} = \lambda_{l1} \mathcal{L}_{l1} + \lambda_{ssim} \mathcal{L}_{ssim} + \lambda_o \mathcal{L}_o \quad (18)$$

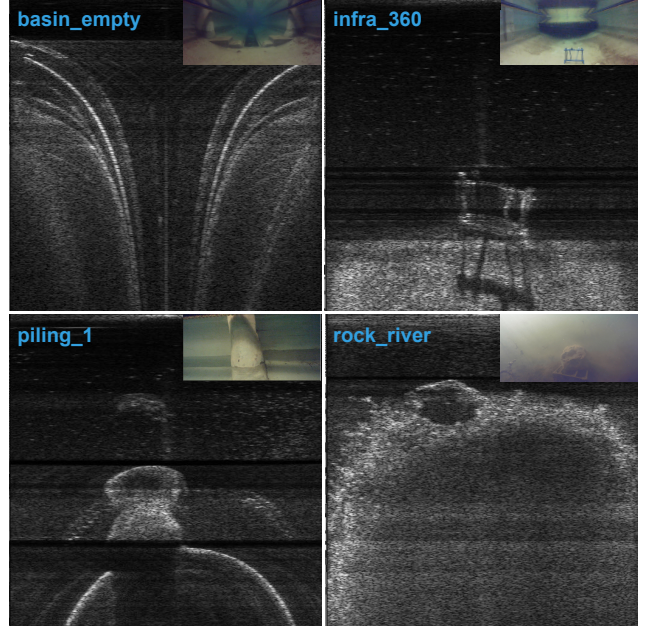


Figure 4. We present selected images from our diverse set of 8 sequences used to evaluate of our method. We show RGB images of the environment for visualization, and captured range/azimuth sonar images. Our evaluation datasets focus on smaller objects and larger-scale structures such as the test-tank basin. Sonar images are polar (range/azimuth).

where λ_{l1} , λ_{ssim} , and λ_o are the weights for the L1, SSIM, and opacity losses respectively.

4. Results & Experiments

4.1. Datasets

We note that real, public datasets of posed sonar images suitable for novel view synthesis experiments do not exist. Rather, we collect sequences using our robotic platform based on a BlueRobotics BlueROV2 vehicle shown in Fig. 1. Our robotic platform is equipped with a BluePrint Subsea Oculus M750-d imaging sonar capable of capturing data across various ranges with a 130° horizontal field of view and a 20° vertical field of view. We use this platform to collect 8 trajectories inspecting a range of objects and in both a test tank and river environment. Fig. 4 shows selected sequences for visualization. For detailed information about sonar parameters, sensor pose estimation, our platform, and dataset details, please refer to the supplemental material.

4.2. Baselines

For baselines, we compare to Neusis [30], Neusis-NGP [44], DSC [7], and ZSplat*. Note that ZSplat [32] was originally designed for camera-sonar fusion. Since we are focused on sonar-only rendering, we compare to a modified version, ZSplat*, trained with the sonar loss.

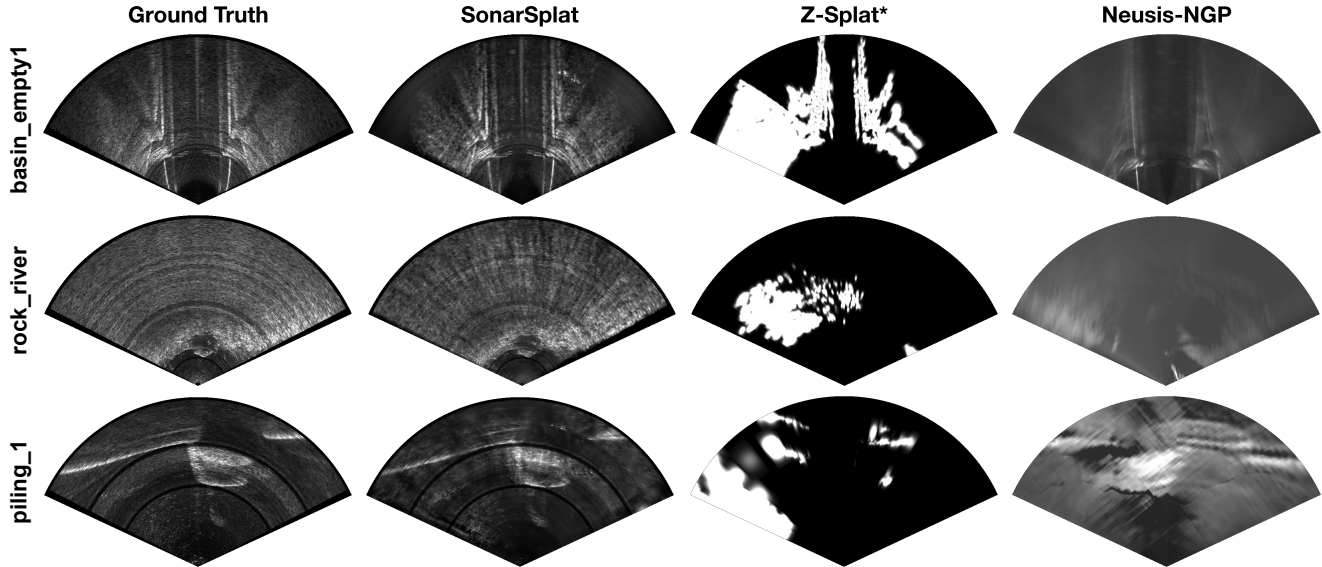


Figure 5. We present qualitative novel view synthesis results from selected datasets and baselines. Note that SonarSplat produces superior sonar image synthesis compared to baselines and is better able to capture finer details in the environment. SonarSplat is also able to capture azimuth streaking phenomena, which no other baseline is able to do. We increase the brightness for all outputs by 25% for easier viewing. Note that Z-Splat* indicates Z-Splat trained only with the sonar loss. Images are cartesian.

Sequence	De-Streaking Performance (ICV) (\uparrow)		
	Captured Image	SonarSplat NVS	De-Streaked Image
basin_empty	2.74	9.78	19.44
infra_360	2.89	34.30	44.18
piling_1	2.78	11.47	19.51
basin_infra	2.77	4.41	4.84
rock_360	2.86	25.00	44.47
piling_2	2.79	7.61	10.32
pole_river	3.11	2.69	2.78
rock_river	3.15	5.15	6.78
Average	2.89	12.55	19.04

Table 1. Quantitative results for azimuth streak removal. We report the inverse coefficient of variation (ICV) [37]. Higher is better (\uparrow), and best is in **bold**.

4.3. Novel View Synthesis

We train our method on an NVIDIA RTX 3090 GPU with 24 GB of vRAM. For detailed implementation details, please refer to the supplemental material. We report validation PSNR, SSIM, and LPIPS following [13, 21]. For our validation set, we take every 8th image from the dataset as introduced in [21]. We report SonarSplat’s performance compared to baselines in Tab. 2. We find that SonarSplat consistently synthesizes more realistic sonar images, quantified by its higher PSNR, SSIM, and lower LPIPS values. We also present qualitative results from selected sequences in Fig. 5. Note that these qualitative results are in cartesian space for interpretability. For extensive polar image results, please refer to the supplemental material. Finally, we explore the feasibility of SonarSplat for data synthesis appli-

Method	Sonar Image Synthesis		
	PSNR (\uparrow)	SSIM (\uparrow)	LPIPS (\downarrow)
Neusis [30]	14.43	0.03	0.66
Neusis-NGP [44]	19.43	0.33	0.55
DSC [7]	14.87	0.10	0.63
Z-Splat* [32]	8.57	0.03	0.68
SonarSplat (ours)	21.89	0.41	0.62

Table 2. Novel view synthesis performance on real world data. Note that ZSplat* is ZSplat with only the sonar loss activated for training. Best is shown in **bold**.

cations by reporting the rendering speed in frames per second (FPS) of each method in Tab. 3. We calculate the FPS of each method on an NVIDIA A6000 GPU with 50 GB of vRAM. SonarSplat and ZSplat both leverage Gaussian splatting, which offers significantly faster rendering speeds compared to neural rendering methods. ZSplat is optimized for high rendering speed, which will be a focus of future work for SonarSplat.

4.4. Azimuth Streak Removal

Since SonarSplat learns probabilities of azimuth streaking for each Gaussian, we can undo the adaptive gain to render images without azimuth streaks present and recover suppressed returns. This vision task is most similar to *image de-stripping* from the remote sensing literature. We present quantitative results in Tab. 1 using the inverse coefficient of variation (ICV) metric, which is a common no-reference

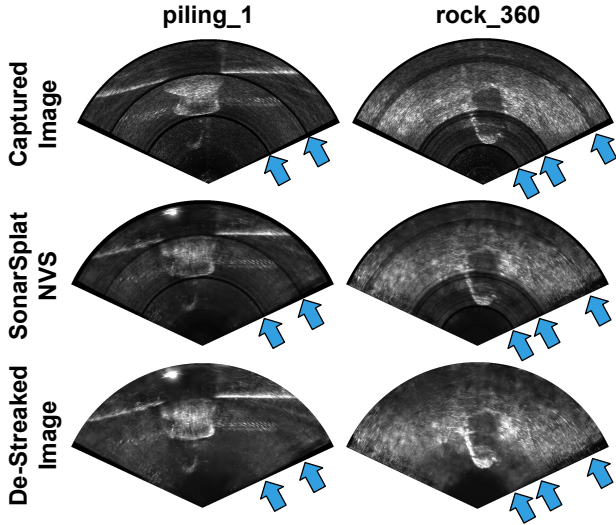


Figure 6. Qualitative results for azimuth streak removal capabilities of SonarSplat. Note that other baselines are unable to remove azimuth streaks from synthesized images since they do not learn the streaking parameters. Locations of azimuth streaks in the captured images are shown in blue arrows for illustrative purposes. SonarSplat is able to effectively restore sonar imagery that exhibits azimuth streaking. Images are cartesian.

Rendering Speed (\uparrow)	
Method	FPS
Neusis [30]	0.03
Neusis-NGP [44]	0.01
DSC [7]	0.03
Z-Splat* [32]	155.32
SonarSplat (ours)	9.46

Table 3. Rendering speed in frames per second (FPS) averaged across all validation images across all sequences. All results are reported on an NVIDIA RTX A6000 GPU. Note that ZSplat* is ZSplat with only sonar rendering. Best is shown in **bold**.

metric used in de-stripping works [26, 33, 36, 37]. We present qualitative results of de-streaked images in Fig. 6.

4.5. 3D Reconstruction

We show that SonarSplat learns the geometric properties of the scene by converting the optimized splat into a pointcloud for visualization. We compare with methods focusing on 3D reconstruction: Neusis and DSC [7, 30]. Qualitative results are shown in Fig. 7 and quantitative results are shown in Tab. 4. We use popular metrics from scene reconstruction literature and choose l_1 Chamfer Distance, F-Score, and voxelized IoU to evaluate performance [1]. For Neusis and DSC, we produce meshes using marching cubes. For SonarSplat, we choose to sample points from the 3D Gaussians to produce a pointcloud. We sample 100,000 points from both the mesh and Gaussian splat and compute

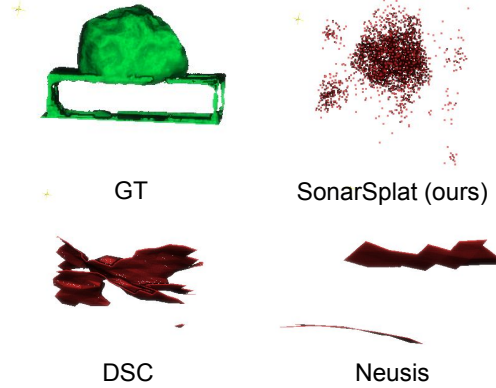


Figure 7. Qualitative results from 3D reconstruction of SonarSplat compared to baselines.

Method	Reconstruction Metrics		
	CD- l_1 (m) \downarrow	F-Score \uparrow	IoU \uparrow
Neusis [30]	0.202	0.4834	0.0129
DSC [7]	0.187	0.4613	0.0164
SonarSplat (ours)	0.084	0.1170	0.0191

Table 4. We quantitatively evaluate the 3D reconstruction of selected methods on the `rock_360` sequence. Best is in **bold**.

evaluation metrics against a ground truth photogrammetry reconstruction of the rock platform. We note that neither Neusis nor DSC are able to reconstruct the object whereas SonarSplat is able to produce a coarse representation.

5. Conclusion & Future Work

We propose SonarSplat, the first sonar-only Gaussian splatting framework for novel view synthesis for imaging sonar in underwater applications. First, we adapt the sonar rendering equation for efficient range-azimuth splatting by evaluating 3D Gaussians. We model azimuth streaking within the Gaussian splatting framework, allowing us to learn per-Gaussian azimuth streaking probabilities and produce high-quality de-streaked images. We perform experiments on real-world data in test tank and river environments. In the novel view synthesis task, SonarSplat outperforms baselines by +2.5 dB PSNR and demonstrates superior qualitative results. We also demonstrate that SonarSplat learns scene geometry, demonstrated by both quantitative and qualitative results. Future work will focus on leveraging SonarSplat for sonar data synthesis by randomizing scene parameters including acoustic reflectance and azimuth streaking probability. This can yield more diverse datasets for training sonar-based scene understanding algorithms. We will also work to improve SonarSplat’s ability to perform dense 3D reconstruction by better modeling additional acoustic phenomena like speckle noise, Lambertian scattering, and multi-path reflections.

6. Acknowledgment

This work is supported by the National Science Foundation under Award No. 2337774.

References

- [1] Dejan Azinović, Ricardo Martin-Brualla, Dan B Goldman, Matthias Nießner, and Justus Thies. Neural rgb-d surface reconstruction. In *Proceedings of the IEEE/CVF Conference on Computer Vision and Pattern Recognition (CVPR)*, pages 6290–6301, 2022. 8
- [2] Jonathan T. Barron, Ben Mildenhall, Matthew Tancik, Peter Hedman, Ricardo Martin-Brualla, and Pratul P. Srinivasan. Mip-nerf: A multiscale representation for anti-aliasing neural radiance fields, 2021. 2
- [3] David Borts, Erich Liang, Tim Broedermann, Andrea Ramazzina, Stefanie Walz, Edoardo Palladin, Jipeng Sun, David Brueggemann, Christos Sakaridis, Luc Van Gool, Mario Bijelic, and Felix Heide. Radar fields: Frequency-space neural scene representations for fmew radar. In *ACM SIGGRAPH 2024 Conference Papers*, New York, NY, USA, 2024. Association for Computing Machinery. 2
- [4] Alexandra Carlson, Manikandasriram S. Ramanagopal, Nathan Tseng, Matthew Johnson-Roberson, Ram Vasudevan, and Katherine A. Skinner. Cloner: Camera-lidar fusion for occupancy grid-aided neural representations. *IEEE Robotics and Automation Letters*, 8(5):2812–2819, 2023. 2
- [5] Rômulo Cerqueira, Tiago Trocoli, Gustavo Neves, Sylvain Joyeux, Jan Albiez, and Luciano Oliveira. A novel gpu-based sonar simulator for real-time applications. *Computers & Graphics*, 68:66–76, 2017. 2
- [6] W. Chen, W. Yifan, S. Kuo, and G. Wetzstein. Dehazenerf: Multiple image haze removal and 3d shape reconstruction using neural radiance fields. In *3DV*, 2024. 1, 2
- [7] Yunxuan Feng, Wenjie Lu, Haowen Gao, Binyu Nie, Kaiyang Lin, and Liang Hu. Differentiable space carving for 3d reconstruction using imaging sonar. *IEEE Robotics and Automation Letters*, 9(11):10065–10072, 2024. 2, 3, 4, 6, 7, 8
- [8] Yunhao Ge, Harkirat Behl, Jiashu Xu, Suriya Gunasekar, Neel Joshi, Yale Song, Xin Wang, Laurent Itti, and Vibhav Vineet. Neural-sim: Learning to generate training data with nerf. *arXiv preprint arXiv:2207.11368*, 2022. 2
- [9] Thomas Guerneve, Kartic Subr, and Yvan Petillot. Three-dimensional reconstruction of underwater objects using wide-aperture imaging sonar. *Journal of Field Robotics*, 35(6):890–905, 2018. 2
- [10] Tianshu Huang, John Miller, Akarsh Prabhakara, Tao Jin, Tarana Laroia, Zico Kolter, and Anthony Rowe. Dart: Implicit doppler tomography for radar novel view synthesis, 2024. 2
- [11] Tiffany A. Huang and Michael Kaess. Towards acoustic structure from motion for imaging sonar. In *2015 IEEE/RSJ International Conference on Intelligent Robots and Systems (IROS)*, pages 758–765, 2015. 2, 4
- [12] Hordur Johannsson, Michael Kaess, Brendan Englot, Franz Hover, and John Leonard. Imaging sonar-aided navigation for autonomous underwater harbor surveillance. In *2010 IEEE/RSJ International Conference on Intelligent Robots and Systems*, pages 4396–4403. IEEE, 2010. 1, 2
- [13] Bernhard Kerbl, Georgios Kopanas, Thomas Leimkühler, and George Drettakis. 3d gaussian splatting for real-time radiance field rendering. *ACM Transactions on Graphics*, 42(4), 2023. 2, 4, 5, 6, 7
- [14] Pou-Chun Kung, Xianling Zhang, Katherine A. Skinner, and Nikita Jaipuria. Lihi-gs: Lidar-supervised gaussian splatting for highway driving scene reconstruction, 2024. 4
- [15] Deborah Levy, Amit Peleg, Naama Pearl, Dan Rosenbaum, Derya Akkaynak, Simon Korman, and Tali Treibitz. SeaThru-NeRF: Neural Radiance Fields in Scattering Media. In *Proceedings of the IEEE/CVF Conference on Computer Vision and Pattern Recognition*, pages 56–65, 2023. 2, 6
- [16] Huapeng Li, Wenxuan Song, Tianao Xu, Alexandre Elsig, and Jonas Kulhanek. WaterSplatting: Fast underwater 3D scene reconstruction using gaussian splatting. *arXiv*, 2024. 2
- [17] Yvette Y Lin, Xin-Yi Pan, Sara Fridovich-Keil, and Gordon Wetzstein. ThermalNeRF: Thermal radiance fields. In *IEEE International Conference on Computational Photography (ICCP)*. IEEE, 2024. 2
- [18] Jonathon Luiten, Georgios Kopanas, Bastian Leibe, and Deva Ramanan. Dynamic 3d gaussians: Tracking by persistent dynamic view synthesis. In *3DV*, 2024. 2
- [19] Hidenobu Matsuki, Riku Murai, Paul H. J. Kelly, and Andrew J. Davison. Gaussian Splatting SLAM. 2024. 2
- [20] John McConnell, John D. Martin, and Brendan Englot. Fusing concurrent orthogonal wide-aperture sonar images for dense underwater 3d reconstruction. In *2020 IEEE/RSJ International Conference on Intelligent Robots and Systems (IROS)*, pages 1653–1660, 2020. 1
- [21] Ben Mildenhall, Pratul P. Srinivasan, Matthew Tancik, Jonathan T. Barron, Ravi Ramamoorthi, and Ren Ng. Nerf: Representing scenes as neural radiance fields for view synthesis, 2020. 2, 7
- [22] Ben Mildenhall, Pratul P. Srinivasan, Matthew Tancik, Jonathan T. Barron, Ravi Ramamoorthi, and Ren Ng. NeRF: Representing Scenes as Neural Radiance Fields for View Synthesis. In *Computer Vision – ECCV 2020*, pages 405–421, Cham, 2020. Springer International Publishing. 1
- [23] Nir Mualem, Roy Amoyal, Oren Freifeld, and Derya Akkaynak. Gaussian splashing: Direct volumetric rendering underwater. *arXiv*, 2024. 2
- [24] Thomas Müller, Alex Evans, Christoph Schied, and Alexander Keller. Instant neural graphics primitives with a multi-resolution hash encoding. *ACM Trans. Graph.*, 41(4):102:1–102:15, 2022. 2
- [25] S. Negahdaripour. On 3-d reconstruction from stereo fs sonar imaging. In *OCEANS 2010 MTS/IEEE SEATTLE*, pages 1–6, 2010. 2
- [26] Janet Elizabeth Nichol and Vijay Vohora. Noise over water surfaces in landsat tm images. *International Journal of Remote Sensing*, 25(11):2087–2093, 2004. 8
- [27] Naama Pearl, Tali Treibitz, and Simon Korman. Nan: Noise-aware nerfs for burst-denoising. In *CVPR*, 2022. 1, 2

- [28] Easton Potokar, Spencer Ashford, Michael Kaess, and Joshua G. Mangelson. HoloOcean: An underwater robotics simulator. In *2022 International Conference on Robotics and Automation (ICRA)*, pages 3040–3046, 2022. [2](#)
- [29] E. Potokar, K. Lay, K. Norman, D. Benham, T. Neilsen, M. Kaess, and J.G. Mangelson. HoloOcean: Realistic sonar simulation. In *Proc. IEEE/RSJ Intl. Conf. on Intelligent Robots and Systems, IROS*, Kyoto, Japan, 2022. [2](#), [5](#), [6](#)
- [30] Mohamad Qadri, Michael Kaess, and Ioannis Gkioulekas. Neural implicit surface reconstruction using imaging sonar, 2022. [2](#), [3](#), [4](#), [6](#), [7](#), [8](#)
- [31] Mohamad Qadri, Kevin Zhang, Akshay Hinduja, Michael Kaess, Adithya Pediredla, and Christopher A. Metzler. Aoneus: A neural rendering framework for acoustic-optical sensor fusion, 2024. [2](#), [4](#)
- [32] Ziyuan Qu, Omkar Vengurlekar, Mohamad Qadri, Kevin Zhang, Michael Kaess, Christopher Metzler, Suren Jayasuriya, and Adithya Pediredla. Z-splat: Z-axis gaussian splatting for camera-sonar fusion, 2024. [2](#), [3](#), [6](#), [7](#), [8](#)
- [33] Preesan Rakwatin, Wataru Takeuchi, and Yoshifumi Yasuoka. Stripe noise reduction in modis data by combining histogram matching with facet filter. *IEEE Transactions on Geoscience and Remote Sensing*, 45(6):1844–1856, 2007. [8](#)
- [34] Advait V. Sethuraman, Anja Sheppard, Onur Bagoren, Christopher Pinnow, Jamey Anderson, Timothy C. Havens, and Katherine A. Skinner. Machine learning for shipwreck segmentation from side scan sonar imagery: Dataset and benchmark. *The International Journal of Robotics Research*, 0(0):02783649241266853, 0. [1](#)
- [35] Advait Venkatraman Sethuraman, Manikandasriram Srinivasan Ramanagopal, and Katherine A. Skinner. Waternerf: Neural radiance fields for underwater scenes, 2023. [2](#)
- [36] Huanfeng Shen and Liangpei Zhang. A map-based algorithm for destriping and inpainting of remotely sensed images. *IEEE Transactions on Geoscience and Remote Sensing*, 47(5):1492–1502, 2008. [8](#)
- [37] GM Smith and Paul Curran. Methods for estimating image signal-to-noise ratio (snr). 1999. [7](#), [8](#)
- [38] Matias Valdenegro-Toro. Submerged marine debris detection with autonomous underwater vehicles. In *2016 International Conference on Robotics and Automation for Humanitarian Applications (RAHA)*, pages 1–7. IEEE, 2016. [2](#)
- [39] Jinkun Wang, Fanfei Chen, Yewei Huang, John McConnell, Tixiao Shan, and Brendan Englot. Virtual maps for autonomous exploration of cluttered underwater environments. In *IEEE Journal of Oceanic Engineering*. IEEE, 2022. [2](#)
- [40] Yusheng Wang, Chujie Wu, Yonghoon Ji, Hiroshi Tsuchiya, Hajime Asama, and Atsushi Yamashita. 2d forward looking sonar simulation with ground echo modeling, 2024. [2](#)
- [41] E. Westman and M. Kaess. Wide aperture imaging sonar reconstruction using generative models. In *Proc. IEEE/RSJ Intl. Conf. on Intelligent Robots and Systems, IROS*, pages 8067–8074, Macao, 2019. [4](#)
- [42] Eric Westman, Ioannis Gkioulekas, and Michael Kaess. A volumetric albedo framework for 3d imaging sonar reconstruction. In *2020 IEEE International Conference on Robotics and Automation (ICRA)*, pages 9645–9651, 2020. [2](#)
- [43] Yiping Xie, Nils Bore, and John Folkesson. Sidescan only neural bathymetry from large-scale survey. *Sensors*, 22(14), 2022. [2](#)
- [44] Yiping Xie, Giancarlo Troni, Nils Bore, and John Folkesson. Bathymetric surveying with imaging sonar using neural volume rendering. *IEEE Robotics and Automation Letters*, 9(9): 8146–8153, 2024. [2](#), [3](#), [6](#), [7](#), [8](#)
- [45] Daniel Yang, John J. Leonard, and Yogesh Girdhar. Seasplat: Representing underwater scenes with 3d gaussian splatting and a physically grounded image formation model. *arxiv*, 2024. [2](#)